OPEN

NPG Asia Materials (2016) 8, e338; doi:10.1038/am.2016.191
www.nature.com/am

ORIGINAL ARTICLE

Restoration of thermally reduced graphene oxide by atomic-level selenium doping

Young Soo Yun[1,2], Gabin Yoon[1], Min Park[3], Se Youn Cho[4], Hee-Dae Lim[1], Haegyeom Kim[1], Yung Woo Park[3], Byung Hoon Kim[5], Kisuk Kang[1,6] and Hyoung-Joon Jin[4]

The use of reduced graphene oxide (rGO) suffers from irreparable damage because of topological defects and residual heteroatoms, which degrade the inherent properties of graphene. To restore its electrical transport properties, charge-transfer chemical doping with *d*-electron-rich heteroatoms has been proposed. Herein, we report the effects of atomic-level selenium doping in rGO. Using first-principles calculations, we found that selenium atoms could be selectively bonded in particular locations, such as the pseudo-edge sites of hole-cluster defects in the basal plane and edge defect sites of graphene; however, we found that the intrinsic topological defects of the basal plane were unfavorable for bonding. Numerous selenium atoms were introduced on the fully amorphorized rGO surface, inducing a dramatic change of its electrical transport properties by electron doping. The large metallic regions formed by the selenium atoms on rGOs led to the enhancement of electrical conductivity by 210 S cm^{-1} at 300 K. Moreover, the temperature-dependent conductivities (σ)/σ_{20K} of selenium-doped rGOs (Se-rGOs) were almost constant in the temperature range of 20–300 K, indicating that the carrier mobility of Se-rGOs becomes temperature-independent after selenium doping, similar to that of pure graphene.
NPG Asia Materials (2016) **8,** e338; doi:10.1038/am.2016.191; published online 16 December 2016

INTRODUCTION

Graphene has attracted much attention in physics, chemistry and materials science because of its unique characteristics, such as high electrical conductivity (~10^6 S cm^{-1}), high intrinsic mobility (200 000 cm^2 V^{-1} s^{-1}), large Young's modulus (~1.0 TPa), and exceptional thermal conductivity (~5000 W m^{-1} K^{-1}).[1–3] However, the practical application of graphene is limited because of the difficulty of its large-scale production. Therefore, a chemical route has been established for producing the so-called graphene oxide (GO).[3–5] GO possesses numerous topological defects and oxygen heteroatoms that distinguish it from pure graphene, and it cannot be restored to its initial state even via healing by various reduction processes. The large number of sp^3 sites and residual oxygen groups of reduced GO (rGO) negatively affect the intrinsic properties of graphene.[6–8] Hence, it is indispensable to endow rGO with properties similar to those of graphene.

Chemical doping with heteroatoms or molecules that can increase the density of free charge carriers in rGO is expected to enhance its electrical conductivity.[9–13] Charge-transfer chemical doping of graphene can be subdivided into surface transfer doping and substitutional doping.[11] In general, surface transfer doping does not destroy the graphene structure and is thus reversible. In contrast, substitutional doping refers to the permanent substitution of carbon atoms in the aromatic hexagonal lattice of graphene. Surface transfer doping occurs via charge transfer from the adsorbed dopant to graphene, and is closely related to their density of states (DOS). Therefore, adsorption of electron-withdrawing molecules leads to *p*-type doping, while the adsorption of electron-donating molecules induces *n*-type doping. Similarly, the *p*- or *n*-type doping can be induced by substitution with dopants having fewer or more valence electrons, respectively. A large number of studies have reported substitutional doping by nitrogen,[9,10,14,15] boron,[14–16] sulfur[17–20] and phosphorus[20–23] in carbon-based materials. These types of dopants affect the carbon crystalline structure by acting as defects, while providing the free charge carrier density and electroactive surface properties. In addition, surface transfer doping has been performed using *p*-type dopants such as NO_2, Br_2 and I_2 vapors,[24–28] and *n*-type dopants such as K and Rb,[27–31] leading to greatly enhanced electrical properties. Nevertheless, since these dopants exhibit air-instability and toxicity, their use in practical applications is limited.

Selenium is a polyatomic, nonmetallic chalcogen with a large atom size (located in the period 4 along with potassium and bromine) and high polarizability, and is *d*-electron-rich (located in group 16).[32] Because of these characteristics, selenium is a promising potential

[1]Department of Materials Science and Engineering, Seoul National University, Seoul, Korea; [2]Department of Chemical Engineering, Kangwon National University, Samcheok, Korea; [3]Department of Physics and Astronomy, Seoul National University, Seoul, Korea; [4]Department of Polymer Science and Engineering, Inha University, Incheon, Korea; [5]Department of Physics, Incheon National University, Incheon, Korea and [6]Center for Nanoparticle Research, Institute for Basic Science (IBS)
Correspondence: Professor K Kang, Department of Materials Science and Engineering, Seoul National University, 1 Gwanak-ro, Gwanak-gu, Seoul 151-742, Korea.
E-mail: matlgen1@snu.ac.kr
or Professor H-J Jin, Department of Polymer Science and Engineering, Inha University, 100 Inharo, Nam-gu, Incheon 402-751, Korea.
E-mail: hjjin@inha.ac.kr
Received 2 May 2016; revised 19 September 2016; accepted 25 October 2016

dopant for enhancing electrical transport properties of rGOs. A number of studies have recently reported the catalytic effects of selenium-doped carbon materials in the oxygen reduction,[33,34] as well as electrooxidation of methanol[35] and ethanol.[36] Although these results showed the existence of direct chemical bonding between selenium and carbon, the exact configuration of selenium and its effects on the intrinsic properties of carbon materials are still veiled. Further applications of selenium-doped carbon materials are possible only after a deeper understanding of the role of selenium in carbon host structures.

In this study, we report atomic-level selenium doping and its effects on rGOs. Selenium-doped rGOs (Se-rGOs) were prepared by heating of GO with elemental selenium powder above the sublimation temperature (>685 °C) of selenium. The *d*-electron-rich selenium atoms were homogeneously introduced on the entire rGO surface, leading to greatly improved electrical transport properties caused by the *n*-type doping. As a result, the carrier mobility of rGOs was dramatically restored by the introduced selenium, reaching a value comparable to that of graphene. This study not only provides a fundamental understanding of selenium doping of rGOs but also shows their potential for energy storage applications.

METHODS

Preparation of Se-rGO

GO was prepared from natural graphite (Sigma-Aldrich, St Louis, MO, USA) using the Hummers method.[18] Aqueous GO suspensions were frozen in liquid nitrogen and freeze-dried at −50 °C and 0.045 mbar for 72 h using a lyophilizer (LP3, Jouan, France). After lyophilization, low-density and loosely packed GO powders were obtained. A mixture of the as-obtained lyophilized GO powder (100 mg) and selenium powder (300 mg) was heated in a tubular furnace from room temperature to 800 °C at a heating rate of 10 °C min^{-1}, and the temperature was held for 2 h. An Ar flow rate of 200 ml min^{-1} was used. The obtained product (Se-rGO) was stored in a vacuum oven at 30 °C. rGO was prepared using the same procedure without the elemental selenium powder.

Material characterization

The morphologies of Se-rGO were observed by atomic force microscopy (AFM, NT-MDT, Russia) with an NSG-10 cantilever (NT-MDT, Russia) in semi-contact operation mode and FE-transmission electron microscopy (TEM; JEM-ARM-200F, JEOL, USA). The chemical states of Se-rGO were investigated by X-ray photoelectron spectroscopy (XPS; PHI 5700 ESCA) using monochromated Al K_α radiation ($h\nu = 1486.6$ eV). Elemental analysis was performed using an elemental analysis1112 instrument (CE instrument, Italy). Raman measurements were performed using an NTEGRA Spectra spectrometer (NT-MDT, Russia) equipped with a 473 nm (2.62 eV) laser in backscattering configuration. The spectral resolution was ~2 cm^{-1} with a 600 groove per mm grating. A ×100 objective (NA = 0.9) provided a laser spot of ca. 330 nm diameter. The laser power was kept well below 0.3 mW for nondestructive Raman measurements.

Computational details

All geometric optimizations and DOS calculations were conducted using Vienna *ab initio* simulation package software[37] of the density functional theory framework. We used a plane-wave basis set with a kinetic energy cutoff of 500 eV and a projector-augmented wave pseudopotential[38] provided by Vienna *ab initio* simulation package. A generalized gradient approximation suggested by Perdew–Burke–Ernzerhof[39] was adopted for the correction of exchange correlation energy. We constructed a model graphene structure containing 72 and 192 carbon atoms in a single layer for the calculation of the adsorption energies. To describe the edge site adsorption, a zigzag graphene nanoribbon structure was used, containing the same amount of carbon atoms as the graphene model. A 15-Å vacuum slab was introduced to avoid the interaction between graphene layers. The adsorption energy E_{ad} was defined as

$$E_{ad} = E_{C+Se} - E_C - E_{Se}$$

where E_{C+Se}, E_C, E_{Se} are the free energies of Se-adsorbed graphene, perfect graphene and the chemical potential of Se. For the DOS calculation, 18 *k*-points were uniformly distributed along the graphene nanoribbon, with the structures of the latter being fully relaxed until the system energies converge to <0.05 eV.

Characterization of electronic transport properties

Se-rGO and rGO were dispersed in DMF and deposited on a 300 nm SiO_2/highly *p*-doped Si substrate. Electrode fabrication was performed by standard electron beam lithography, evaporation of Cr/Au (5/120 nm), and lift-off procedures. The temperature dependence of *I*–*V* characteristics was measured using four-probe configurations in a Janis cryogenic system with a current source (6221, Keithley) and nanovoltmeter (2182A, Keithley). The temperature dependence of the conductivity of Se-rGO and rGO was investigated between 20 and 300 K by four-probe measurements using a Keithley 6221/2182A Delta Mode System. Currents of 100 and 10 nA were applied for Se-rGO and rGO, respectively.

Electrochemical characterization

The electrochemical properties of Se-rGO and rGO as anode materials for Li-ion batteries were evaluated using a WonATech automatic battery cycler and CR2032-type coin cells. The working electrodes were prepared by mixing the active material (80 wt.%) with conductive carbon (10 wt.%) and polyvinylidene fluoride (10 wt.%) in *N*-methyl-2-pyrrolidone. The resulting slurries were uniformly applied onto Cu foil. The electrodes were dried at 120 °C for 2 h and roll-pressed. The coin cells were assembled in a glove box filled with argon, employing a composite electrode with metallic lithium foil and 1 M $LiPF_6$ (Aldrich, 99.99%) dissolved in a solution of ethylene carbonate/dimethyl carbonate (1:1 v/v) as the electrolyte. The cells were galvanostatically cycled between 0.01 and 3.0 V vs Li/Li^+ at various current densities.

The air electrode of the Li-air battery was composed of catalyst materials (Se-rGO or rGO) and the polyvinylidene fluoride binder in an 8:2 ratio (w/w). The slurry was prepared using *N*-methyl-2-pyrrolidone and coated on the Ni mesh substrate. Li metal (3/8 inch diameter), a glass fiber separator (Whatman GF/D microfiber filter paper, 2.7 μm pore size), and the prepared air electrodes were assembled in a Swagelok-type cell. 1 M lithium bis(trifluoromethylsulfonyl)imide dissolved in tetraethylene glycol dimethylether was used as an electrolyte. The cells were operated at a constant outer pressure of pure oxygen at 770 Torr.

RESULTS AND DISCUSSION

Se-rGO samples have a thickness of ~15 nm, a lateral size of several micrometers, and numerous ripples on their surface (Figure 1a), indicating morphologies similar to those of rGOs reduced at 800 °C in the absence of elemental selenium (Supplementary Figure S1). TEM and electron energy loss spectroscopy mapping images of Se-rGOs shows that a large amount of selenium atoms were doped on the entire area of the carbon hosts structure of rGOs (Figure 1b–d). Moreover, scanning TEM (STEM) images of Se-rGOs and rGOs show clear differences, namely that Se-rGOs have a relatively rough surface, as indicated by the presence of numerous bright spots (Figure 1e and Supplementary Figure S2). The presence of selenium atoms on the rGO surface (with atomic selenium content of ~13%) is also confirmed by energy-dispersive X-ray spectroscopy (EDS; Supplementary Figure S3). Nevertheless, the high-resolution TEM image (Figure 1f) of Se-rGO shows no aggregates or nanoparticles on its surface, indicating atomic-level selenium doping of rGO. Notably, the carbon structures of Se-rGOs and rGOs were highly amorphorized (Figure 1f and Supplementary Figure S4). Magnified high-resolution TEM images of Se-rGOs also show selenium atoms (Figure 1g). The large *d*-electron-rich selenium atoms (radius: 120 pm) are depicted as bright spots, which are observed on the highly amorphorized Se-rGO

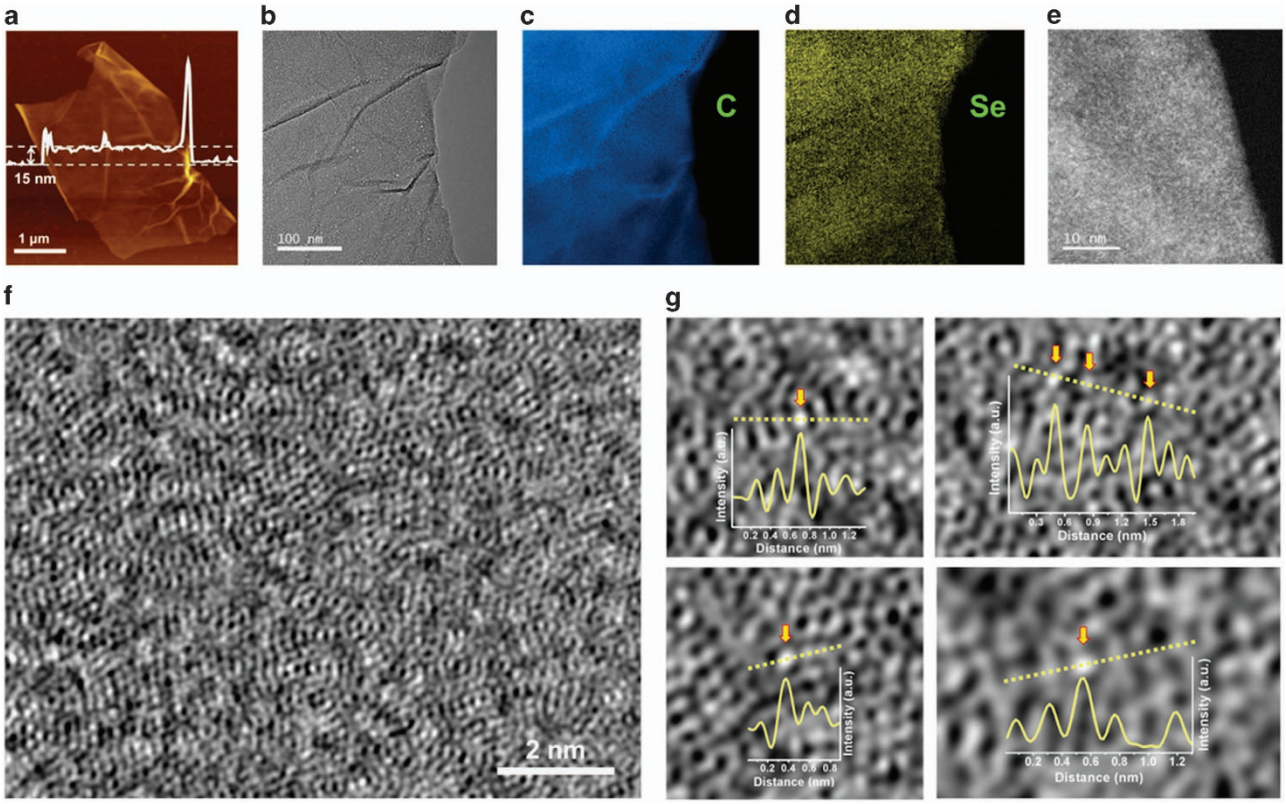

Figure 1 Direct observation of selenium atoms doped on rGO. Topographical images of Se-rGO recorded using (**a**) atomic force microscopy and (**b**) FE-TEM. Se-rGO has a thickness of ~15 nm and a lateral size of several micrometers, exhibiting a high aspect ratio. Electron energy loss spectroscopy (EELS) mapping images of (**c**) carbon and (**d**) selenium. Selenium atoms were homogeneously doped over the whole surface of rGO. (**e**) Scanning transmission electron microscopy image of Se-rGO. Numerous bright spots are observed on the entire surface of Se-rGO. (**f**) High-resolution transmission electron microscopy (HR-TEM) image of Se-rGO, showing its highly amorphorized surface. (**g**) Higher magnification HR-TEM images obtained from **f**. The atoms observed as bright spots, having a larger size than other ones, are considered selenium atoms.

surfaces. The chemical states of Se-rGOs were characterized by XPS (Figure 2a–c). The C 1*s* spectrum shows several distinct peaks due to C–O and C–Se bonds centered at 285.8 eV and the ones due to C=O bonds centered at 290.5 eV. In addition, the spectrum shows the main C–C bond peak centered at 284.5 eV (Figure 2a), which is similar to the value observed for rGOs (Supplementary Figure S5a). Oxygenated functional groups were also found in the O 1*s* spectrum, as indicated by the peaks due to C–O and C=O bonds, centered at 533.3 and 530.5 eV, respectively (Figure 2b). The C/O atomic ratio of Se-rGOs was ~10.9, which was higher than the corresponding value of 9.2 for rGOs, indicating the more reduced nature of Se-rGOs. Selenium atoms were mostly present in the form of C–Se–C bonds, as indicated by the peak centered at 56.3 eV, with peak due to the minor Se–O bonds located at 59.3 eV (Figure 2c), showing that selenium atoms were chemically doped on the rGO surface. The C/Se atomic ratio was calculated as ~40.7, which is much lower than the value suggested by the energy-dispersive X-ray spectroscopy data. To determine the selenium content more accurately, elemental analysis was performed, and we obtained ~15 wt.% selenium content for Se-rGOs, in agreement with the XPS results. In addition, Fourier transform infrared spectroscopy data supports the presence of the C–Se–C bonds (Supplementary Figure S5b). Nevertheless, it is notable that the Raman spectra showed similar *D*/*G* intensity ratios (I_D/I_G), as well as integrated sp^3 and sp^2 area ratios (A_{sp3}/A_{sp2}) for Se-rGO and rGO (Figure 2d, Supplementary Figures S6 and S7). The deconvoluted Raman spectra of Se-rGO and rGO and their integrated area ratios of sp^3 and sp^2 (A_{sp3}/A_{sp2}) are shown in Supplementary Figures S6 and S7.[40] The *D* band corresponds to the disorder in the A_{1g} breathing mode of the six-membered aromatic ring near the basal edge, while the *G* band reflects the hexagonal structure related to the E_{2g} vibration mode of the sp^2-hybridized carbon atoms. Therefore, the similar I_D/I_G values mean that selenium doping slightly affects the hexagonal carbon structure, suggesting that the doping could be close to surface transfer doping.

More specific information on chemical bonding was obtained using density functional theory calculations (Figure 3). Various defect sites of rGOs including intrinsic topological defects, pseudo-edge sites of hole-cluster defects in the basal plane of graphene, and graphene edge defects are considered possible adsorption sites for selenium atoms (Figure 3a). As shown in Figure 3a, configurations 1–5 represent selenium adsorption on top of the carbon atoms (1), C–C bonds (2), carbon rings (3), at the pseudo-edge sites of hole-cluster defects in the graphene basal plane (4), and at the graphene edge defect sites (5; Supplementary Figure S8). The calculated selenium adsorption energies for each adsorption site are given in Figure 3b. Note that multiple points are described for configurations 1–3, since there are several distinctive local environments for selenium adsorption, composed of 5-, 6- and 7-membered carbon rings (see Supporting Information for details). The most stable adsorption sites in configurations 1–3, denoted by red circles in Figure 3b, were the carbon

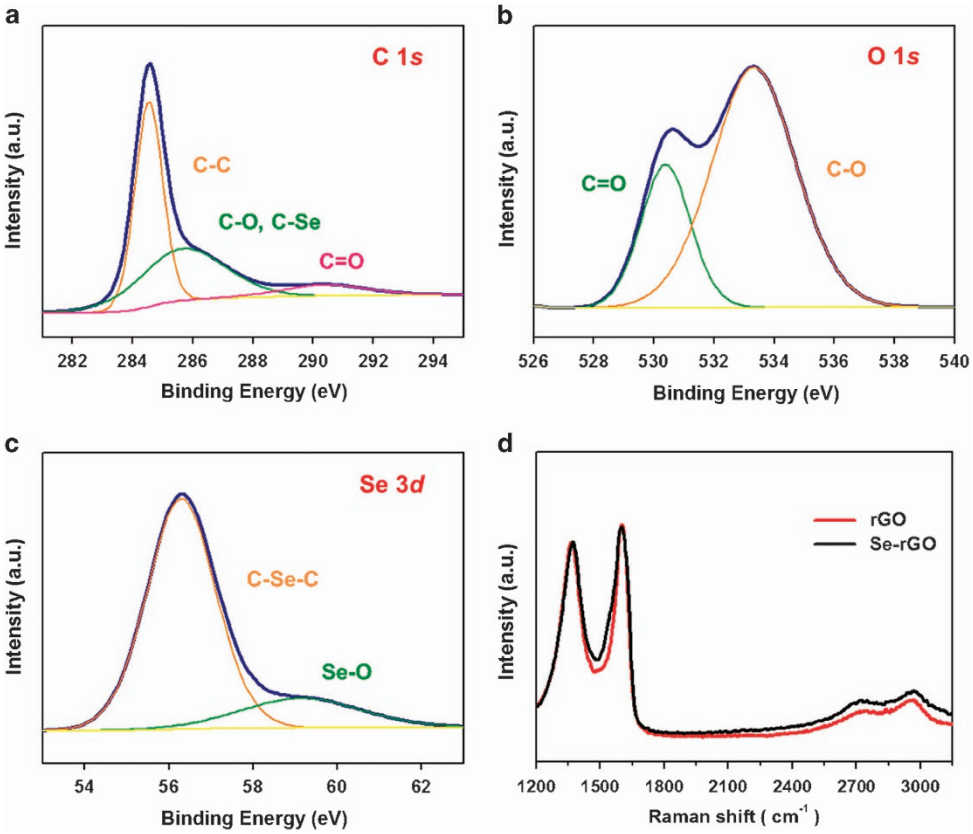

Figure 2 Chemical configuration and microstructure of Se-rGO. (**a**) C 1*s*, (**b**) O 1*s*, (**c**) Se 3*d* X-ray photoelectron spectroscopy spectra of Se-rGO. Se-rGO possesses chalcogen heteroatoms involved in C–O, C=O, C–Se and Se–O bonding. Most of Se atoms are present in the form of C–Se bonds. (**d**) Raman spectra of rGO and Se-rGO. The two Raman spectra are similar, as are their I_D/I_G intensity ratios, indicating that the carbon microstructure was not changed by selenium doping.

atoms 577 of configuration 1, 77 of configuration 2, and the five-membered carbon ring of configuration 3. However, all selenium adsorption energies in configurations 1–3 were positive, indicating that binding of Se atoms at intrinsic topological defect sites such as mono-vacancies, di-vacancies and Stone-Wales defects is unfavorable. These results agree with the previous computational reports on substitutional sulfur doping of graphene[41] and surface sulfur doping of defected graphene,[18] both showing a positive binding energy for sulfur adsorption at the intrinsic defect sites of graphene. On the other hand, the binding energies of selenium atoms at both pseudo-edge hole-cluster defect sites in the basal plane and the edge defect sites of graphene are negative, indicating that Se atoms can be spontaneously bound only at the pseudo-edge and edge defect sites, which are relatively unstable. Moreover, the negative energy of selenium adsorption implies chemical bonding with graphene on an atomic level, not just physical adsorption. We also considered the possibility of selenium adsorption in the presence of oxygenated functional groups (Supplementary Figure S9). We find that selenium atoms are not likely to directly bind with oxygen; however, their individual adsorption is possible in near oxygenated functional groups, in agreement with the XPS result that showed Se–O bonding (Figure 2b). In addition, we calculated the DOS for H- and Se-terminated graphene nanoribbons to investigate the effect of Se doping on electronic properties (Figure 3c and d). The detailed model structures used for DOS calculations are depicted in Supplementary Figure S8e. As shown in Figure 3c and d, the Fermi level of Se-terminated graphene nanoribbons is 0.5 eV higher than that of H-terminated ones. As selenium has more valence electrons than carbon atoms, they are naturally transferred from selenium to rGO, hybridizing with the carbon atoms of rGO and occupying high-energy states, which leads to a positive shift of the Fermi level and makes Se-rGO an *n*-type conducting material. This effect is also reported for doping with K[42] and NH.[43] Since *n*-type doped graphene typically shows increased electrical conductivity due to the introduction of charge carriers[43] Se-rGOs can exhibit improved electrical conductivity compared to rGOs.

Temperature-dependent current–voltage (*I–V*) characterization of rGO and Se-rGO was performed (Figure 4a and b). For both samples, the *I–V* curves show highly symmetric and linear behavior in all temperature regions, with the slope of *I–V* curves increasing concomitantly with temperature. The curves indicate an increase in conductivity with temperature. Interestingly, the current of Se-rGO is two orders of magnitude higher than that of rGO, and the *I–V* curve slope for Se-rGO changes little, despite the temperature variation from 20 to 300 K. For detailed observations, the temperature-dependent conductivities ($\sigma(T)$) of rGO and Se-rGO were obtained as the temperature was continuously varied from 20 to 300 K (Figure 4c). The $\sigma(T)$ of Se-rGO is larger than that of rGO by 1–2 orders of magnitude. The defects and functional groups cause an increase of dipole polarization, thus, reducing the conduction path length in GO.[44] For rGO, the dipole polarization is reduced by the decreased amount of defects and oxygenated functional groups, which increase

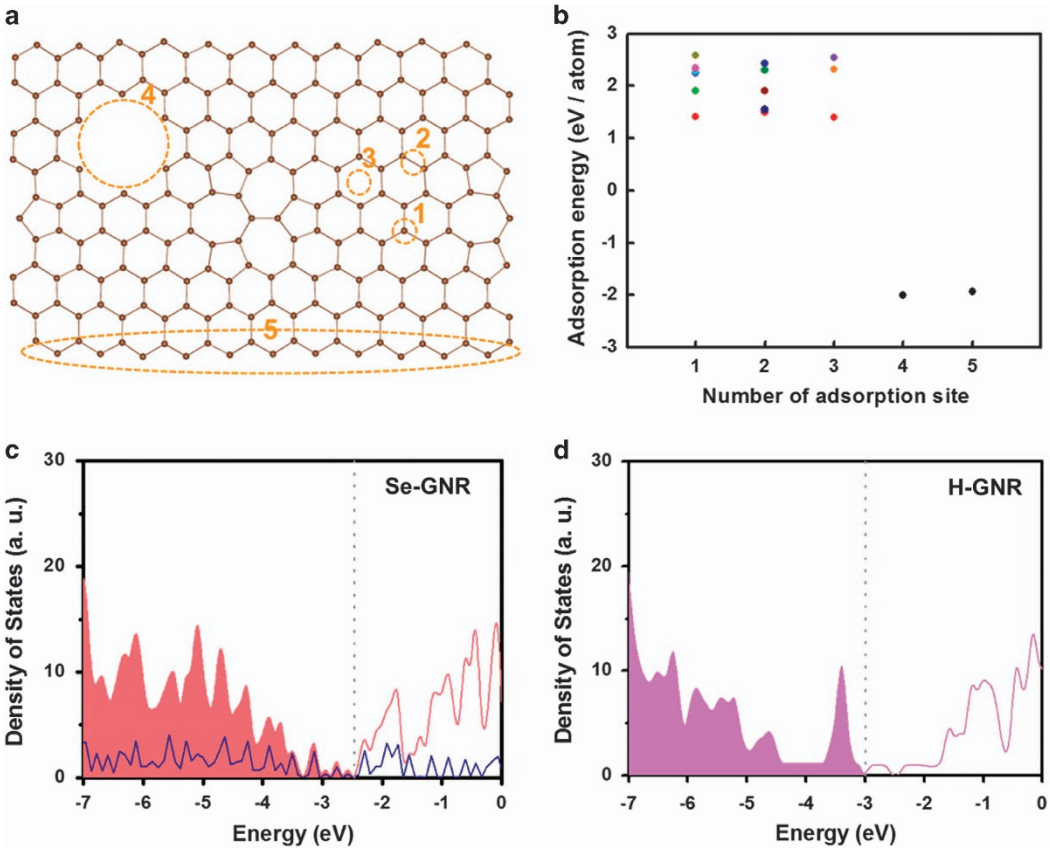

Figure 3 Density functional theory calculations for the configuration of selenium on rGO. (**a**) Various possible adsorption sites on defected graphene (1 – atom, 2 – bridge, 3 – ring center, 4 – hole defect, and 5 – edge) and (**b**) Se adsorption energies thereon. (**c**) DOS of Se-terminated GNR (scarlet) and PDOS of Se (navy), and (**d**) DOS of H-terminated GNR. The dashed lines in **c**, **d** indicate the Fermi level, while the occupied energy levels are filled in color.

the probability of electron hopping. Hence, the electronic transport mechanism of rGO has been attributed to variable hopping.[45] The rGO follows the Efros–Shklovskii variable-range hopping ($\sigma = \sigma_0 \exp(-T_0/T)^{1/2}$, where σ_0 and T_0 are 87.8 S cm^{-1} and 508.2 K, respectively), which is known for the transport properties of rGO with different fractions of sp^2 carbon (blue color in Figure 4c).[46] However, the electrical transport properties of Se-rGO were not fitted by the Efros–Shklovskii variable-range hopping model, but were well explained by the fluctuation-induced tunneling mechanism[47] (red color in Figure 4c). The $\sigma(T)$ in the fluctuation-induced tunneling model is expressed as $\sigma = \sigma_\infty \exp(-T_1/(T+T_0))$, where T_0 and T_1 are 200 and 96 K, respectively. T_0 is the onset temperature of thermally activated conduction, and T_1 is a measure of the energy required for an electron to cross the insulator gap between conductive regions. These values indicate that Se-rGO possesses large metallic regions separated by a relatively small insulating gap. These metallic regions created by selenium doping increase the conductivity to 210 S cm^{-1} at 300 K, a very large conductivity value compared to that of rGO (obtained using N_2H_4, ~2 S cm^{-1})[45] and is comparable to the ultrahigh bulk conductivity of GO papers reduced by metal iodides.[48] Note that the variation of $\sigma(T)$ in Se-rGO is quite small (Figure 4d). The $\sigma/\sigma_{20\ K}$ value of rGO increases 41.5-fold as the temperature increases from 20 to 300 K, while that of Se-rGO stays almost constant (1.3-fold increase from 20 to 300 K). This means that the carrier mobility becomes temperature-independent because of selenium doping; the carrier mobility being similar to that of pure graphene.[49]

Furthermore, the effects of selenium doping on the electrical transport properties of monolayer rGO were directly investigated by *in situ* measurements at 300 K (Supplementary Figure S10). The sample was loaded in a doping tube, with selenium powder placed on the bottom. The tube containing the sample was evacuated using a rotary pump ($<3\times10^{-2}$ Torr; Supplementary Figure S10a). As the bottom of the tube was heated, the conductivity of rGO abruptly increased from 0.27 to 0.58 S cm^{-1} and then saturated (Supplementary Figure S10b). Moreover, we also studied the gate voltage (V_G)-dependent conductivity at 300 K, observing graphene-like field-effect behavior. The minimum conductivity (σ_{min}) of rGO was located near $V_G = 60$ V (Supplementary Figure S10c). However, this value shifted toward negative V_G after selenium doping, implying that this doping was *n*-type. Based on the electrical transport properties, we conclude that the chemisorbed selenium atoms on rGO result in electron doping of the latter, enhancing its electrical conductivity.

The superior electrical transport properties of Se-rGOs lead to significantly enhanced electrochemical properties of energy storage systems. As an anode material for Li-ion batteries, Se-rGOs show a much higher rate performance as well as an increased capacity, as compared to rGO (Figure 5a–c). The reversible capacity of Se-rGO equals 570 mAh g^{-1} at a current density of 1 C (372 mA g^{-1}; Figure 5a), which is much higher than the value of 310 mAh g^{-1}, observed for rGO (Figure 5a). The enhanced capacity of Se-rGO suggests that selenium atoms contribute to the reversible Li-ion storage, as supported by the change of galvanostatic discharge/charge

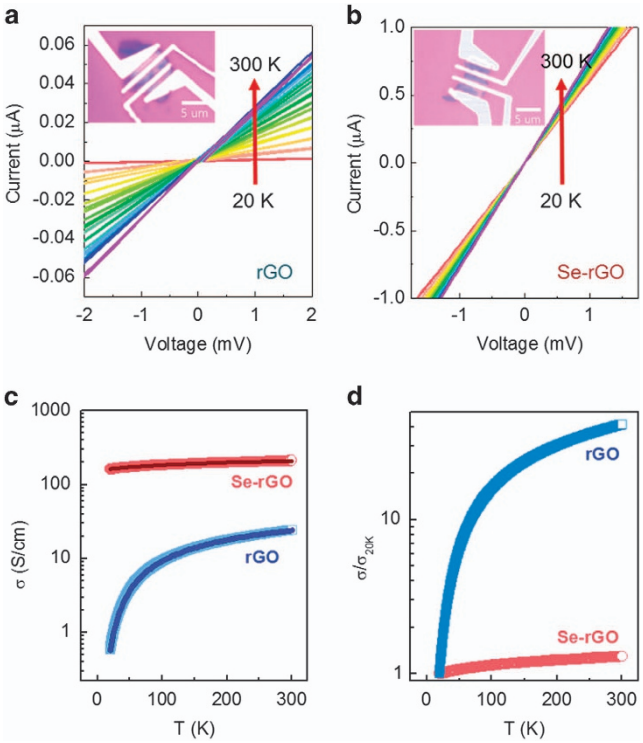

Figure 4 Temperature-dependent electron transport properties of rGO and Se-rGO. Temperature-dependent electrical transport properties of (**a**) rGO and (**b**) Se-rGO measured between 20 and 300 K in 20-K steps with inset optical images of the four-electrode configurations. The slope of the *I–V* curves increased concomitantly with temperature, indicating an increase of conductivity with temperature. (**c**) Temperature dependence of rGO and Se-rGO conductivities obtained from *I–V* curves and variable-range hopping (VRH) and fluctuation-induced tunneling (FIT) models. rGO and Se-rGO were well-fitted by VRH and FIT models, respectively. (**d**) Temperature vs $\sigma/\sigma_{20\ K}$ plots for rGO and Se-rGO. The above curve for Se-rGO is almost flat in the temperature range from 20 to 300 K (1.3-fold increase), indicating that the carrier mobility becomes temperature-independent due to selenium doping, implying mobility restoration.

profiles. The same test conducted at low temperature (0 °C) shows a more distinct capacity gap between Se-rGO and rGO, as displayed in Supplementary Figure S11. In the low-temperature cell test, the reversible capacity of Se-rGO is 360 mAh g^{-1}, corresponding to ~63% of the capacity at 25 °C. In contrast, rGO shows a reversible capacity of ~140 mAh g^{-1}, corresponding to ~45% of that at 25 °C. These results suggest that the enhanced electrical properties of Se-rGO affect its electrochemical performance at low temperature to a great extent. Highly stable capacities of 165 mAh g^{-1} could be obtained at a large current rate of 50 C, which is approximately seven times higher than the value of rGO anode materials (Figure 5b). In addition, the high rate performance of Se-rGO is significant compared to graphene-based electrode materials and nitrogen-doped graphene nanosheets for Li-ion batteries.[50,51] After 200 cycles with a consecutive increase of current density from 1 C (372 mA g^{-1}) to 50 C (18,600 mA g^{-1}), the specific capacity of Se-rGO returns to its initial value of ca. 460 mAh g^{-1}, indicating good reversibility. In addition, cycling stability is found to be maintained during 1000 repetitive cycles, showing a Coulombic efficiency of nearly 100% (Figure 5c).

We thought that Se-rGO could be a potential catalyst material for Li–O_2 batteries because of its high-energy density. However, we found that such batteries suffered from large polarization during charging, resulting in poor cycling stability (Figure 5d and e). The above behavior was due to the formation of non-conductive Li_2O_2 during discharge. When a conventional ether-based electrolyte (that is, tetraethylene glycol dimethylether) was used for Li–O_2 batteries, amorphous Li_2O_2 entangled on the carbon surface and bulk crystalline Li_2O_2 with toroidal morphology were both observed simultaneously. The preference between amorphous and crystalline Li_2O_2 is significantly affected by the properties of the electrolyte, current rates, and depth of discharge.[52,53] In the fully discharged state, as shown in Figure 5d, nucleated Li_2O_2 has enough time to grow into large toroidal particles with high crystallinity. Based on theoretical studies of the charge transport properties of bulk Li_2O_2, its intrinsic ionic and electronic conductivities were calculated as ~10^{-19} S cm^{-1}, which is unacceptably low for charge conduction.[54] Therefore, despite the enhanced electrical conductivity, the charge profile of Se-rGO showed a large polarization similar to that of rGO because of the low conductivity of the large toroidal Li_2O_2 particles. In this respect, a particular electrochemical protocol should be used to clearly demonstrate the effect of Se-rGO in Li–O_2 cells. Thus, we used capacity-limited discharge to produce surface-derived Li_2O_2. Since the surface-derived Li_2O_2 directly comes into contact with the Se-rGO surface, the enhanced electrical properties of Se-rGO could highly affect the charge polarization of Li–O_2 cells. As shown in Figure 5e, the air cells tested under a protocol, wherein the discharge capacity was limited to 500 mA h g^{-1}, show an obvious difference in their charge profiles. Overall, the Se-rGO-based electrode showed a lower charge potential than rGO; in particular, the initial part (~200 mA h g^{-1}) had a charge potential below 4.0 V. Based on this result, we could verify the effect of selenium doping in rGO. Additionally, when a soluble LiI catalyst was used, the Se-rGO-based electrode showed an abrupt decrease of charge polarization near 0.5 V (Figure 5e), which was superior to the previous reports on rGO electrodes in terms of energy efficiency.[55–57] These results, thus, demonstrate the possibility of using Se-rGO-based electrodes for Li–O_2 batteries.

CONCLUSION

In this work, we investigated the effects of selenium doping in rGO. Numerous selenium atoms were homogeneously doped on the top surface of rGOs; it caused little structural change, indicative of surface transfer doping. high-resolution TEM images showed no aggregates or nanoparticles on the surface of rGOs, indicating that selenium atoms were introduced in an atomic level. Based on first-principles calculations, we found the selenium atoms to be mainly bonded to the surface edge defect sites of highly amorphorized rGO, leading to the enhancement of electrical conductivity due to *n*-type doping. In contrast, the overall intrinsic topological defects of the graphene basal plane showed an unfavorable selenium atom binding energy. The doped selenium atoms changed the electrical transport properties of rGO. The properties were well fitted by the fluctuation-induced tunneling mechanism, and the results indicated the presence of a large metallic region separated by a relatively small insulating gap. The σ value of Se-rGO reached 210 S cm^{-1} at 300 K, while the $\sigma/\sigma_{20\ K}$ parameter was almost constant (1.3-fold increase from 20 to 300 K), this indicated that the carrier mobility of Se-rGO was similar to that of graphene. In addition, Se-rGO showed a superior electrochemical performance as an anode for Li-ion batteries and a catalyst for Li–O_2 batteries because of the effects of selenium doping in rGO.

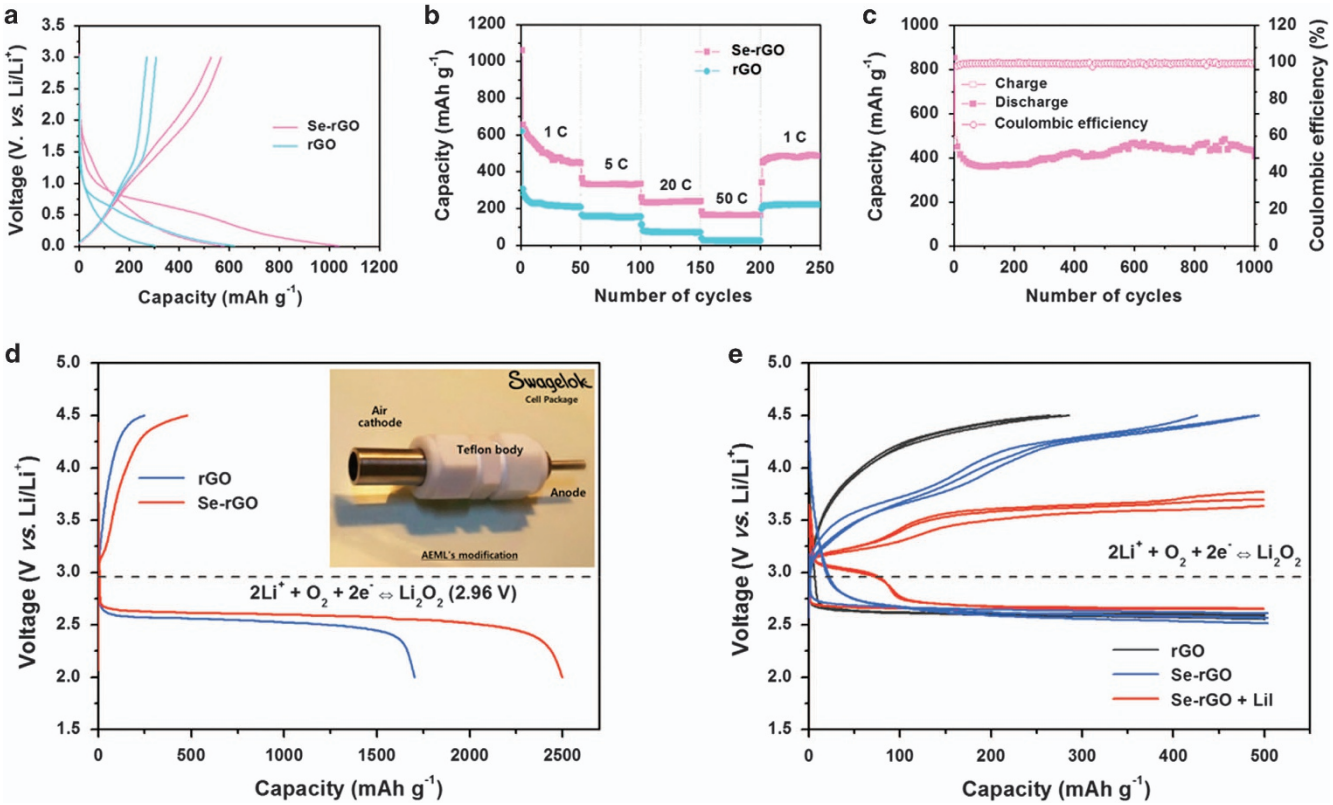

Figure 5 Electrochemical performances of rGO and Se-rGO as the anode and catalyst for Li-ion and Li-air batteries, respectively. (**a**) Galvanostatic discharge/charge profiles of Se-rGO and rGO at a current density of 1 C (372 mA g^{-1}), (**b**) rate performances of Se-rGO and rGO at consecutively increasing current densities from 1 C (372 mA g^{-1}) to 50 C (18 600 mA g^{-1}), with subsequent reversal to 1 C (372 mA g^{-1}), and (**c**) cycling performance of Se-rGO as a Li-ion battery anode for 1000 repetitive cycles at a current density of 3 C (1116 mA g^{-1}). (**d**) Discharge/charge profiles of rGO- and Se-rGO-based air electrodes in a potential range of 2.0–4.5 V at a constant current rate of 200 mA g^{-1} for Li–O_2 cells (inset image of a modified Li–O_2 Swagelok-type cell). (**e**) Comparison of electrochemical properties for rGO- and Se-rGO-based Li–O_2 cell air electrodes with and without the LiI catalyst. The capacity was utilized up to 500 mAh g^{-1}. The dotted line indicates the theoretical formation voltage of Li_2O_2 at 2.96 V vs Li/Li^+.

CONFLICT OF INTEREST

The authors declare no conflict of interest.

ACKNOWLEDGEMENTS

This work was supported by the World Premier Materials grant funded by the Korea government Ministry of Trade, Industry and Energy. This work was also supported by the Graphene Materials/Components Development Project (10044366, Fabrication of the hybrid graphene barrier film with OTR/WVTR (10^{-6} cc(g)/m^2 day) grade for commercialized package, photovoltaic and display technology) funded By the Ministry of Trade, industry & Energy (MI, Korea) and Basic Science Research Program through the National Research Foundation of Korea (NRF) funded by the Ministry of Education (NRF-2016R1A2B4009601).

Author contributions: This research was guided by KK and H-JJ. Sample preparation and analyses were performed by YSY, SYC, MP, YWP and BHK carried out electrical measurements. GY carried out first-principles calculations. H-DL and HK assisted with electrochemical characterization. YSY wrote the manuscript.

1 Geim, A. K. Graphene: status and prospects. *Science* **324**, 1530–1534 (2009).
2 Geim, A. K. & Novoselov, K. S. The rise of graphene. *Nat. Mater.* **6**, 183–191 (2007).
3 Zhu, Y., Murali, S., Cai, W., Li, X., Suk, J. W., Potts, J. R. & Ruoff, R. S. Graphene and graphene oxide: synthesis, properties, and applications. *Adv. Mater.* **22**, 3906–3924 (2010).
4 Dreyer, D. R., Park, S., Bielawski, C. W. & Ruoff, R. S. The chemistry of graphene oxide. *Chem. Soc. Rev.* **39**, 228–240 (2010).
5 Bianco, A., Cheng, H.-M., Enoki, T., Gogotsi, Y., Hurt, R. H., Koratkar, N., Kyotani, T., Monthioux, M., Park, C. R., Tascon, J. M. D. & Zhang, J. All in the Graphene Family – a recommended nomenclature for two-dimensional carbon materials. *Carbon* **65**, 1–6 (2013).
6 Bagri, A., Mattevi, C., Acik, M., Chabal, Y. J., Chhowalla, M. & Shenoy, V. B. Structural evolution during the reduction of chemically derived graphene oxide. *Nat. Chem.* **2**, 581–587 (2010).
7 Gómez-Navarro, C., Meyer, J. C., Sundaram, R. S., Chuvilin, A., Kurasch, S., Burghard, M., Kern, K. & Kaiser, U. Atomic structure of reduced graphene oxide. *Nano Lett.* **10**, 1144–1148 (2010).
8 Erickson, K., Erni, R., Lee, Z., Alem, N., Gannett, W. & Zettl, A. Determination of the local chemical structure of graphene oxide and reduced graphene oxide. *Adv. Mater.* **22**, 4467–4472 (2010).
9 Wang, X., Li, X., Zhang, L., Yoon, Y., Weber, P. K., Wang, H., Guo, J. & Dai, H. N-doping of graphene through electrothermal reactions with ammonia. *Science* **324**, 768–771 (2009).
10 Zhao, L., He, R., Rim, K. T., Schiros, T., Kim, K. S., Zhou, H., Gutiérrez, C., Chockalingam, S. P., Arguello, C. J., Pálová, L., Nordlund, D., Hybertsen, M. S., Reichman, D. R., Heinz, T. F., Kim, P., Pinczuk, A., Flynn, G. W. & Pasupathy, A. N. Visualizing individual nitrogen dopants in monolayer graphene. *Science* **333**, 999–1003 (2011).
11 Giovannetti, G., Khomyakov, P. A., Brocks, G., Karpan, V. M., Brink, J. V. D. & Kelly, P. J. Doping graphene with metal contacts. *Phys. Rev. Lett.* **101**, 026803 (2008).
12 Liu, H., Liu, Y. & Zhu, D. Chemical doping of graphene. *J. Mater. Chem.* **21**, 3335–3345 (2011).
13 Ristein, J. Surface transfer doping of semiconductors. *Science* **313**, 1057–1058 (2006).
14 Biel, B., Blase, X., Triozon, F. & Roche, S. Anomalous doping effects on charge transport in graphene nanoribbons. *Phys. Rev. Lett.* **102**, 096803 (2009).
15 Lherbier, A., Blase, X., Niquet, Y.-M., Triozon, F. & Roche, S. Charge transport in chemically doped 2D graphene. *Phys. Rev. Lett.* **101**, 036808 (2008).

16 Li, X., Fan, L., Li, Z., Wang, K., Zhong, M., Wei, J., Wu, D. & Zhu, H. Boron doping of graphene for graphene-silicon p-n junction solar cells. *Adv. Energy Mater.* **2**, 425–429 (2012).
17 Yang, Z., Yao, Z., Li, G., Fang, G., Nie, H., Liu, Z., Zhou, X., Chen, X. & Huang, S. Sulfur-doped graphene as an efficient metal-free cathode catalyst for oxygen reduction. *ACS Nano* **6**, 205–211 (2012).
18 Yun, Y. S., Le, V.-D., Kim, H., Chang, S.-J., Baek, S. J., Park, S., Kim, B. H., Kim, Y.-H., Kang, K. & Jin, H.-J. Effects of sulfur doping on graphene-based nanosheets for use as anode materials in lithium-ion batteries. *J. Power Sources* **262**, 79–85 (2014).
19 Poh, H. L., Šimek, P., Sofer, Z. & Pumera, M. Sulfur-doped graphene *via* thermal exfoliation of graphite oxide in H_2S, SO_2 or CS_2 gas. *ACS Nano* **7**, 5262–5272 (2013).
20 Paraknowitsch, J. P. & Thomas, A. Doping carbons beyond nitrogen: an overview of advanced heteroatom doped carbons with boron sulphur and phosphorus for energy applications. *Energy Environ. Sci.* **6**, 2839–2855 (2013).
21 Zhang, C., Mahmood, N., Yin, H., Liu, F. & Hou, Y. Synthesis of phosphorus-doped graphene and its multifunctional applications for oxygen reduction reaction and lithium ion batteries. *Adv. Mater.* **25**, 4932–4937 (2013).
22 Liu, Z.-W., Peng, F., Wang, H.-J., Yu, H., Zheng, W.-X. & Yang, J. Phosphorus-doped graphite layers with high electrocatalytic activity for the O_2 reduction in an alkaline medium. *Angew. Chem.* **123**, 3315–3319 (2011).
23 Latorre-Sánchez, M., Primo, A. & Garcia, H. P-doped graphene obtained by pyrolysis of modified alginate as a photocatalyst for hydrogen generation from water-methanol mixtures. *Angew. Chem. Int. Ed.* **52**, 11813–11816 (2013).
24 Schedin, F., Geim, A. K., Morozov, S. V., Hill, E. W., Blake, P., Katsnelson, M. I. & Novoselov, K. S. Detection of individual gas molecules adsorbed on graphene. *Nat. Mater.* **6**, 652–655 (2007).
25 Jung, N., Kim, N., Jockusch, S., Turro, N. J., Kim, P. & Brus, L. Charge transfer chemical doping of few layer graphenes: charge distribution and band gap formation. *Nano Lett.* **9**, 4133–4137 (2009).
26 Behabtu, N., Young, C. C., Tsentalovich, D. E., Kleinerman, O., Wang, X., Ma, A. W. K., Bengio, E. A., Waarbeek, R. F., Jong, J. J., Hoogerwerf, R. E., Fairchild, S. B., Ferguson, J. B., Maruyama, B., Kono, J., Talmon, Y., Cohen, Y., Otto, M. J. & Pasquali, M. Strong, light, multifunctional fibers of carbon nanotubes with ultrahigh conductivity. *Science* **339**, 182–186 (2013).
27 Lee, R. S., Kim, H. J., Fischer, J. E., Thess, A. & Smalley, R. E. Conductivity enhancement in single-walled carbon nanotube bundles doped with K and Br. *Nature* **388**, 255–257 (1997).
28 Rao, A. M., Eklund, P. C., Bandow, S., Thess, A. & Smalley, R. E. Evidence for charge transfer in doped carbon nanotube bundles from Raman scattering. *Nature* **388**, 257–259 (1997).
29 Chen, J.-H., Jang, C., Adam, S., Fuhrer, M. S., Williams, E. D. & Ishigami, M. Charged-impurity scattering in graphene. *Nat. Phys.* **4**, 377–381 (2008).
30 Bostwick, A., Ohta, T., Seyller, T., Horn, K. & Rotenberg, E. Quasiparticle dynamics in graphene. *Nat. Phys.* **3**, 36–40 (2007).
31 Rauf, H., Pichler, T., Knupfer, M., Fink, J. & Kataura, H. Transition from a Tomonaga-Luttinger liquid to a Fermi liquid in potassium-intercalated bundles of single-wall carbon nanotubes. *Phys. Rev. Lett.* **93**, 096805 (2004).
32 Abouimrane, A., Dambournet, D., Chapman, K. W., Chupas, P. J., Weng, W. & Amine, K. A new class of lithium and sodium rechargeable batteries based on selenium and selenium-sulfur as a positive electrode. *J. Am. Chem. Soc.* **134**, 4505–4508 (2012).
33 Jin, Z., Nie, H., Yang, Z., Zhang, J., Liu, Z., Xu, X. & Huang, S. Metal-free selenium doped carbon nanotube/graphene networks as a synergistically improved cathode catalyst for oxygen reduction reaction. *Nanoscale* **4**, 6455–6460 (2012).
34 Choi, C. H., Chung, M. W., Jun, Y. J. & Woo, S. I. Doping of chalcogens (sulfur and/or selenium) in nitrogen-doped graphene-CNT self-assembly for enhanced oxygen reduction activity in acid media. *RSC Adv.* **3**, 12417–12422 (2013).
35 Wamg, R., Da, H., Wang, H., Ji, S. & Tian, Z. Selenium functionalized carbon for high dispersion of platinum-ruthenium nanoparticles and its effect on the electrocatalytic oxidation of methanol. *J. Power Sources* **233**, 326–330 (2013).
36 Wang, H. & Ma, Q. Selenium and oxygen-containing functional groups for co-functionalization of Vulcan carbon and its applications in ethanol oxidation. *J. Solid State Electrochem.* **19**, 355–360 (2015).
37 Kresse, G. & Furthmüller, J. Efficiency of ab-initio total energy calculations for metals and semiconductors using a plane-wave basis set. *Comput. Mater. Sci.* **6**, 15–50 (1996).
38 Blöchl, P. E. Projector augmented-wave method. *Phys. Rev. B* **50**, 17953–17979 (1994).
39 Perdew, J. P., Burke, K. & Ernzerhof, M. Generalized gradient approximation made simple. *Phys. Rev. Lett.* **77**, 3865–3868 (1996).
40 Zhu, Z., Cheng, F. & Chen, J. Investigation of effects of carbon coating on the electrochemical performance of $Li_4Ti_5O_{12}$/C nanocomposites. *J. Mater. Chem. A* **1**, 9484–9490 (2013).
41 Denis, P. A., Faccio, R. & Mombru, A. W. Is it possible to dope single-walled carbon nanotubes and graphene with sulfur? *ChemPhysChem.* **10**, 715–722 (2009).
42 Chen, J. H., Jang, C., Adam, S., Fuhrer, M. S., Williams, E. D. & Ishigami, M. Charged-impurity scattering in graphene. *Nat. Phys.* **4**, 377–381 (2008).
43 Panchakarla, L. S., Subrahmanyam, K. S., Saha, S. K., Govindaraj, A., Krishnamurthy, H. R., Waghmare, U. V. & Rao, C. N. R. Synthesis, Structure, and Properties of Boron- and Nitrogen-Doped Graphene. *Adv. Mater.* **21**, 4726–4730 (2009).
44 Wen, B., Cao, M., Lu, M., Cao, W., Shi, H., Liu, J., Wang, X., Jin, H., Fang, X., Wang, W. & Yuan, J. Reduced graphene oxide: light-weight and high-efficiency electromagnetic interference shielding at elevated temperatures. *Adv. Mater.* **26**, 3484–3489 (2014).
45 Gómez-Navarro, C., Weitz, R. T., Bittner, A. M., Scolari, M., Mews, A., Burghard, M. & Kern, K. Electronic transport properties of individual chemically reduced graphene oxide sheets. *Nano Lett.* **7**, 3499–3503 (2007).
46 Joung, D. & Khondaker, S. I. Efros-Shklovskii variable-range hopping in reduced graphene oxide sheets of varying carbon sp^2 fraction. *Phys. Rev. B* **86**, 235423 (2012).
47 Sheng, P., Sichel, E. K. & Gittleman, J. I. Fluctuation-induced tunneling conduction in carbon-polyvinylchloride composites. *Phys. Rev. Lett.* **40**, 1197–1200 (1978).
48 Liu, C., Hao, F., Zhao, X., Zhao, Q., Luo, S. & Lin, H. Low temperature reduction of free-standing graphene oxide papers with metal iodides for ultrahigh bulk conductivity. *Sci. Rep.* **4**, 3965 (2014).
49 Dean, C. R., Young, A. F., Meric, I., Lee, C., Wang, L., Sorgenfrei, S., Watanabe, K., Taniguchi, T., Kim, P., Shepard, K. L. & Hone, J. Boron nitride substrates for high quality graphene electronics. *Nat. Nanotechnol.* **5**, 722–726 (2010).
50 Liang, M. & Zhi, L. Graphene-based electrode materials for rechargeable lithium batteries. *J. Mater. Chem.* **19**, 5871–5878 (2009).
51 Wang, H., Zhang, C., Liu, Z., Wang, L., Han, P., Xu, H., Zhang, K., Dong, S., Yao, J. & Cui, G. Nitrogen-doped graphene nanosheets with excellent lithium storage properties. *J. Mater. Chem.* **21**, 5430–5434 (2011).
52 Laoire, C. O., Mukerjee, S. & Abraham, K. M. Influence of nonaqueous solvents on the electrochemistry of oxygen in the rechargeable lithium-air battery. *J. Phys. Chem. C* **114**, 9178–9186 (2010).
53 Fan, W., Cui, Z. & Guo, X. Tracking formation and decomposition of abacus-ball-shaped lithium peroxides in Li–O_2 cells. *J. Phys. Chem. C* **117**, 2623–2627 (2013).
54 Radin, M. D. & Siegel, D. J. Charge transport in lithium peroxide: relevance for rechargeable metal–air batteries. *Energy Environ. Sci.* **6**, 2370–2379 (2013).
55 Chen, Y., Zhang, Q., Zhang, Z., Zhou, X., Zhong, Y., Yang, M., Xie, Z., Wei, J. & Zhou, Z. Two better than one: cobalt-copper bimetallic yolk-shell nanoparticles supported on graphene as excellent cathode catalysts for Li–O_2 batteries. *J. Mater. Chem. A* **3**, 17874–17879 (2015).
56 Liu, S., Zhu, Y., Xie, J., Huo, Y., Yang, H. Y., Zhu, T., Cao, G., Zhao, X. & Zhang, S. Direct growth of flower-like δ-MnO_2 on three-dimensional graphene for high-performance rechargeable Li–O_2 batteries. *Adv. Energy Mater.* **4**, 1301960 (2014).
57 Sun, B., Wang, B., Su, D., Xiao, L., Ahn, H. & Wang, G. Graphene nanosheets as cathode catalysts for lithium-air batteries with an enhanced electrochemical performance. *Carbon* **50**, 727–733 (2012).

Supplementary Information accompanies the paper on the NPG Asia Materials website (http://www.nature.com/am)